



Fermi Gamma-Ray Imaging of a Radio Galaxy

The Fermi-LAT Collaboration

Science **328**, 725 (2010);

DOI: 10.1126/science.1184656

This copy is for your personal, non-commercial use only.

If you wish to distribute this article to others, you can order high-quality copies for your colleagues, clients, or customers by [clicking here](#).

Permission to republish or repurpose articles or portions of articles can be obtained by following the guidelines [here](#).

The following resources related to this article are available online at www.sciencemag.org (this information is current as of November 20, 2012):

Updated information and services, including high-resolution figures, can be found in the online version of this article at:

<http://www.sciencemag.org/content/328/5979/725.full.html>

Supporting Online Material can be found at:

<http://www.sciencemag.org/content/suppl/2010/03/31/science.1184656.DC1.html>

This article appears in the following **subject collections**:

Astronomy

<http://www.sciencemag.org/cgi/collection/astronomy>

Our results demonstrate that hybridization capture arrays can generate data from genomic target regions of megabase size from ancient DNA samples, even when only ~0.2% of the DNA in a sample stems from the endogenous genome. By generating an average coverage of 4- to 5-fold, errors from sequencing and small amounts of human DNA contamination can be minimized. A further approximately 5-fold reduction of errors was achieved here by the enzymatic removal of uracil residues that are frequent in ancient DNA (25). Because the Sidrón 1253 Neandertal library used for this study has been amplified and effectively immortalized, the same library should be able to provide similar-quality data for any other genomic target region, or even the entire single-copy fraction of the Neandertal genome.

References and Notes

1. R. E. Green *et al.*, *Science* **328**, 710 (2010).
2. H. N. Poinar *et al.*, *Science* **311**, 392 (2006).
3. W. Miller *et al.*, *Nature* **456**, 387 (2008).
4. A. W. Briggs *et al.*, *Science* **325**, 318 (2009).
5. J. Krause *et al.*, *Curr. Biol.* **20**, 231 (2010).
6. E. Hodges *et al.*, *Nat. Protoc.* **4**, 960 (2009).
7. E. Hodges *et al.*, *Nat. Genet.* **39**, 1522 (2007).
8. E. W. Sayers *et al.*, *Nucleic Acids Res.* **38** (Database issue), D5 (2010).
9. Materials and methods are available as supporting material on Science Online.
10. A. Rosas *et al.*, *Proc. Natl. Acad. Sci. U.S.A.* **103**, 19266 (2006).
11. T. De Torres *et al.*, *Archaeometry* **10.1111/j.1475-4754.2009.00491.x** (2009).
12. H. M. Cann *et al.*, *Science* **296**, 261 (2002).
13. M. Meyer, M. Kircher, *Cold Spring Harb. Protoc.* **10.1101/pdb.prot5448** (2010).
14. R. E. Green *et al.*, *EMBO J.* **28**, 2494 (2009).
15. J. Krause *et al.*, *Curr. Biol.* **17**, 1908 (2007).
16. W. Enard *et al.*, *Nature* **418**, 869 (2002).
17. F. Vargha-Khadem, D. G. Gadian, A. Copp, M. Mishkin, *Nat. Rev. Neurosci.* **6**, 131 (2005).
18. K. Prüfer *et al.*, *BMC Bioinformatics* **8**, 41 (2007).
19. G. M. Cooper *et al.*, *Genome Res.* **15**, 901 (2005).
20. K. E. Lohmueller *et al.*, *Nature* **451**, 994 (2008).
21. B. Boeckmann *et al.*, *Nucleic Acids Res.* **31**, 365 (2003).
22. C. D. Bustamante *et al.*, *Nature* **437**, 1153 (2005).
23. H. H. Wu, B. Su, *BMC Evol. Biol.* **8**, 192 (2008).
24. J. M. Akey, *Genome Res.* **19**, 711 (2009).
25. A. W. Briggs *et al.*, *Nucleic Acids Res.* **38**, e87 (2010).
26. We thank C. S. Burbano, C. de Filippo, J. Kelso, and D. Reich for helpful comments; M. Kircher, K. Prüfer, and U. Stenzel for technical support; C. D. Bustamante and K. E. Lohmueller for access to human resequencing databases; D. L. Goode and A. Sidow for providing conservation scores; J. M. Akey

for providing coordinates of genome-wide scans for selection; I. Gut for human genotyping; E. Leproust and M. Srinivasan for providing early access to the 1 Million feature Agilent microarrays; and the Genome Center at Washington University for pre-publication use of the orangutan genome assembly (http://genome.wustl.edu/genomes/view/pongo_abelii/). The government of the Principado de Asturias funded excavations at the Sidrón site. J.M.G. was supported by an NSF international postdoctoral fellowship (OISE-0754461) and E.H. by a postdoctoral training grant from the NIH and by a gift from the Stanley Foundation. G.J.H. is an investigator of the Howard Hughes Medical Institute, which together with the Presidential Innovation Fund of the Max Planck Society provided generous financial support. DNA sequences are deposited in the European Bioinformatics Institute short read archive, with accession number ERP000125. The array capture technologies used in this study are the subject of pending patent filings U.S. 60/478, 382 (filed 2003) and U.S. 61/205, 834 (filed 2009), on which G.J.H. and E.H. are listed as inventors.

Supporting Online Material

www.sciencemag.org/cgi/content/full/328/5979/723/DC1
Materials and Methods
Figs. S1 to S4
Tables S1 to S5

8 February 2010; accepted 1 April 2010
10.1126/science.1188046

Fermi Gamma-Ray Imaging of a Radio Galaxy

The Fermi-LAT Collaboration*†

The Fermi Gamma-ray Space Telescope has detected the γ -ray glow emanating from the giant radio lobes of the radio galaxy Centaurus A. The resolved γ -ray image shows the lobes clearly separated from the central active source. In contrast to all other active galaxies detected so far in high-energy γ -rays, the lobe flux constitutes a considerable portion (greater than one-half) of the total source emission. The γ -ray emission from the lobes is interpreted as inverse Compton-scattered relic radiation from the cosmic microwave background, with additional contribution at higher energies from the infrared-to-optical extragalactic background light. These measurements provide γ -ray constraints on the magnetic field and particle energy content in radio galaxy lobes, as well as a promising method to probe the cosmic relic photon fields.

Centaurus A (Cen A) is one of the brightest radio sources in the sky and was among the first identified with a galaxy (NGC 5128) outside of our Milky Way (1). Straddling the bright central source is a pair of extended radio lobes with a total angular extent of $\sim 10^\circ$ (2, 3), which makes Cen A the largest discrete nonthermal extragalactic radio source visible from Earth. At a distance of 3.7 Mpc (4), it is the nearest radio galaxy to Earth, and the implied physical source size is ~ 600 kpc. Such double-lobed radio structures associated with otherwise apparently normal giant elliptical galaxies have become the defining feature of radio galaxies in general. The

consensus explanation for this phenomenon is that the lobes are fueled by relativistic jets produced by accretion activity in a super-massive black hole residing at the galaxy's center.

With its unprecedented sensitivity and imaging capability (per-photon resolution: $\theta_{68} \approx 0.8 E_{\text{GeV}}^{-0.8}$), the Fermi Large Area Telescope (LAT) (5) has detected and imaged the radio lobes of Cen A in high-energy γ -rays. The LAT image resulting from ~ 10 months of all-sky survey data (Fig. 1) clearly shows the γ -ray peak coincident with the active galactic nucleus detected by the Compton/EGRET instrument (6) and extended emission from the southern giant lobe. Because the northern lobe is characterized by lower surface-brightness emission (in radio), it is not immediately apparent from a naked-eye inspection of the γ -ray counts map. Nevertheless, from a counts profile extracted along the north-south axis of the source (Fig. 2), γ -ray excesses from both lobes are clearly visible.

Spectra for each of the lobes together with the central source (hereafter referred to as the "core") were determined with a binned maximum likelihood analysis implemented in GTLIKE (7) using events from 0.2 to 30 GeV in equal logarithmically spaced energy bins. We modeled background emission by including the Galactic diffuse component, an isotropic component, and nearby γ -ray point sources [see the supporting online material (SOM)]. We fit the core as a point source at the known radio position and modeled the lobe emission with a 22-GHz Wilkinson Microwave Anisotropy Probe (WMAP) image (Fig. 1) (8) with the core region within a 1° radius excluded as a spatial template. The modeled lobe region roughly corresponds to the regions 1 and 2 (north) and 4 and 5 (south) defined in (9), where region 3 is the core (Fig. 2). Assuming a power law for the γ -ray spectra, we find a large fraction ($>1/2$) of the total >100 -MeV emission from Cen A to originate from the lobes with the flux in each of the northern $\{[0.77(+0.23/-0.19)_{\text{stat.}}(+0.39)_{\text{syst.}}] \times 10^{-7} \text{ ph cm}^{-2} \text{ s}^{-1}\}$ and southern $\{[1.09(+0.24/-0.21)_{\text{stat.}}(+0.32)_{\text{syst.}}] \times 10^{-7} \text{ ph cm}^{-2} \text{ s}^{-1}\}$ lobes smaller than the core flux $\{[1.50(+0.25/-0.22)_{\text{stat.}}(+0.37)_{\text{syst.}}] \times 10^{-7} \text{ ph cm}^{-2} \text{ s}^{-1}\}$ (stat., statistical; syst., systematic). Uncertainties in the LAT effective area, the Galactic diffuse model used, and the core exclusion region were considered to be sources of systematic error (SOM). The resultant test statistic (10) for the northern and southern giant lobes are 29 and 69, which correspond to detection significances of 5.0σ and 8.0σ , respectively. The lobe spectra are steep, with photon indices $\Gamma = 2.52(+0.16/-0.19)_{\text{stat.}}(+0.25)_{\text{syst.}}$ (north) and $2.60(+0.14/-0.15)_{\text{stat.}}(+0.20)_{\text{syst.}}$ (south) in which photons up to ~ 2 to 3 GeV are currently detected. These values are consistent with that of the core [$\Gamma = 2.67(\pm 0.10)_{\text{stat.}}(\pm 0.08)_{\text{syst.}}$], which

*All authors with their affiliations appear at the end of this paper.

†To whom correspondence should be addressed. E-mail: Teddy.Cheung.ctr@nrl.navy.mil (C.C.C.); fukazawa@hep01.hepl.hiroshima-u.ac.jp (Y.F.); jurgen.knodlseder@cesr.fr (J.K.); stawarz@slac.stanford.edu (L.S.)

Fig. 1. (A and B) Fermi-LAT γ -ray (>200 MeV) counts maps centered on Cen A, displayed with square-root scaling. In both (A) and (B), models of the galactic and isotropic emission components were subtracted from the data (in contrast to the observed counts profile presented in Fig. 2). The images are shown before (A) and after (B) additional subtraction of field point sources (SOM) and are shown adaptively smoothed with a minimum signal-to-noise ratio of 10. In (B), the white circle with a diameter of 1° is approximately the scale of the LAT point-spread function width. (C) For comparison, the 22-GHz radio map from the 5-year WMAP data set (8) with a resolution of $0^\circ.83$ is shown. J2000, equinox; h, hour; m, minutes.

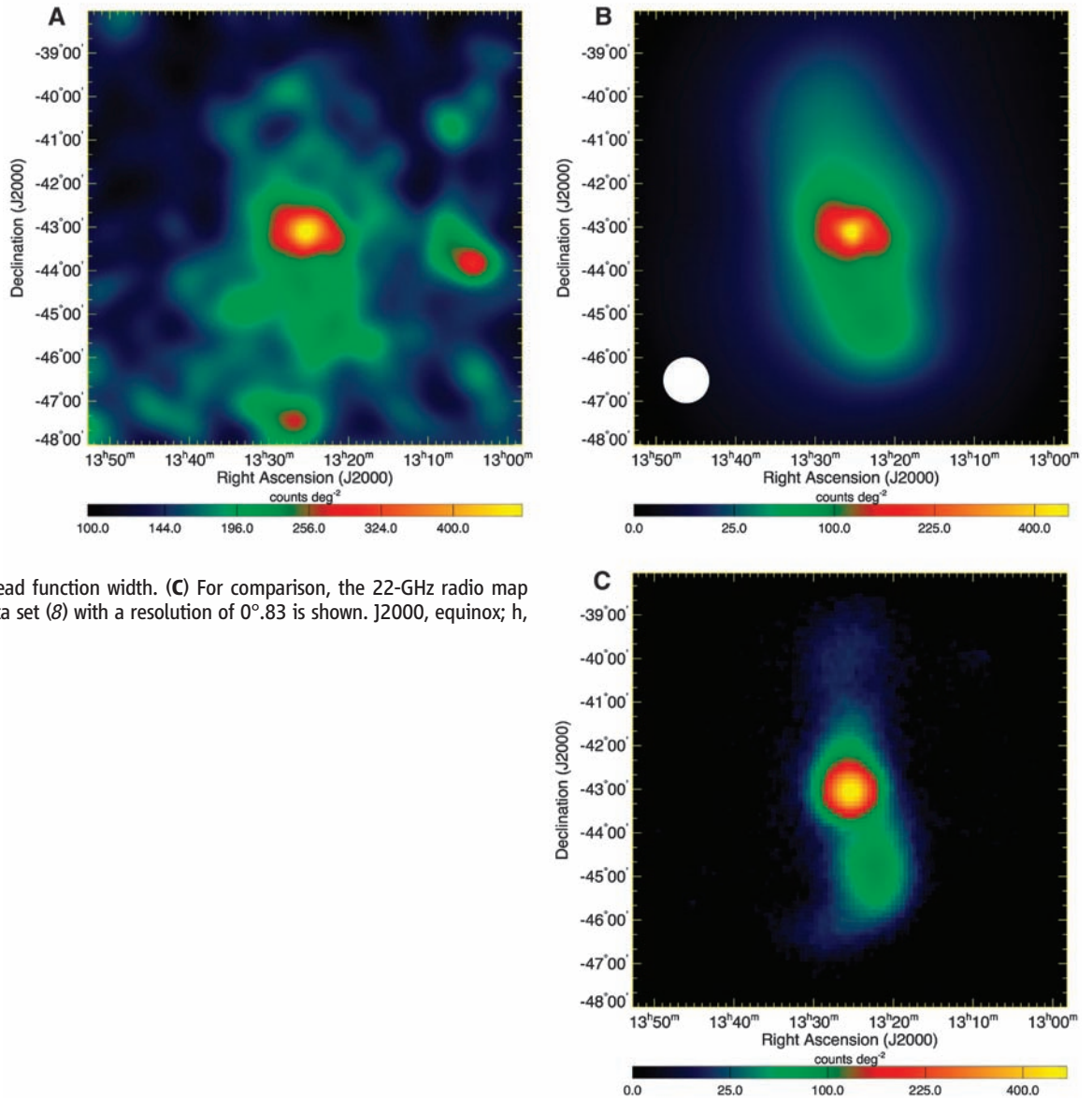
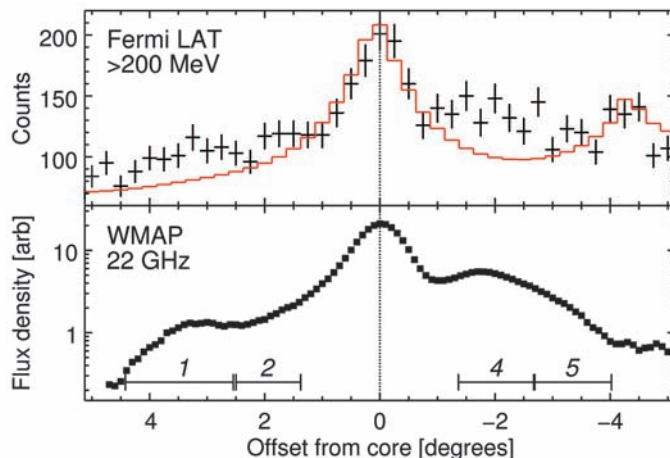


Fig. 2. Observed intensity profiles of Cen A along the north-south axis in γ -rays (top) and in the radio band (bottom). In the bottom panel, the lobe regions 1 and 2 (northern lobe) and regions 4 and 5 (southern lobe) are indicated as in (9), where region 3 (not displayed here) is the core. The red curve overlaid onto the LAT data indicates the emission model for all fitted point sources, plus the isotropic and Galactic diffuse (brighter to the south) emission. The point sources include the Cen A core (offset = 0°) and a LAT source (offset = -4.5°) (see SOM) that is clearly outside (1° from the southern edge) of the southern lobe. The excess counts are coincident with the northern and southern giant lobes. arb, arbitrary units.



is known to have a steep γ -ray spectrum (6). For further details pertaining to the analysis of the lobe emission, see the SOM.

It is well-established that radio galaxy lobes are filled with magnetized plasma containing ultra-relativistic electrons emitting synchrotron radiation in the radio band (observed frequencies: $\nu \sim 10^7$ to 10^{11} Hz). These electrons also up-scatter ambient photons to higher energies via the inverse Compton (IC) process. At the observed distances far from the parent galaxy (>100 -kpc scale), the dominant soft-photon field surrounding the extended lobes is the pervading radiation from the cosmic microwave background (CMB) (11). Because IC/CMB scattered emission in the lobes of more distant radio galaxies is generally well observed in the x-ray band (12–14), the IC spectrum can be expected to extend to even higher energies (9, 15), as demonstrated by the LAT detection of the Cen A giant lobes.

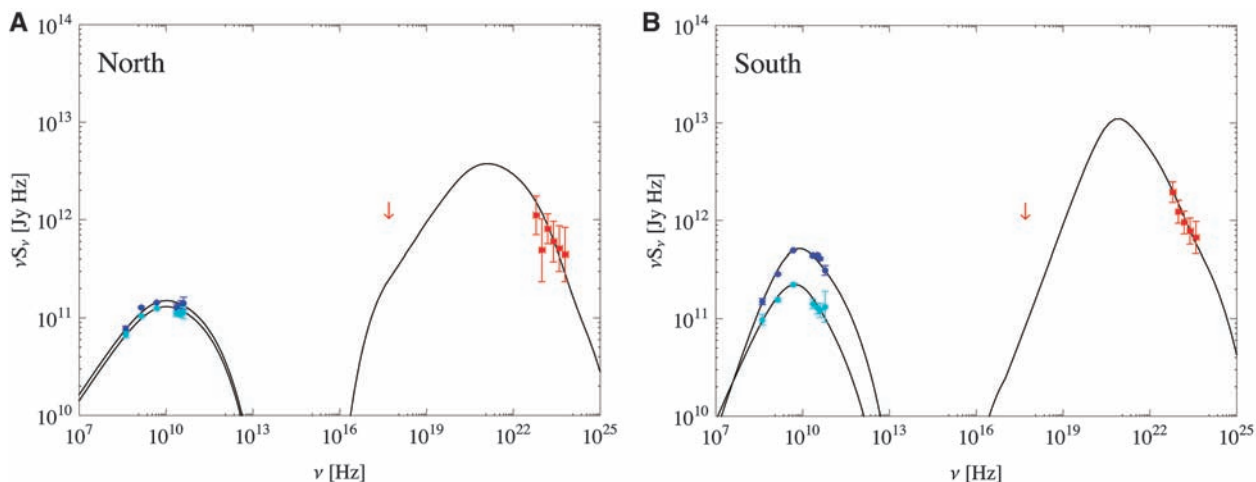


Fig. 3. Broad-band SEDs of the northern (**A**) and southern (**B**) giant lobes of Cen A. The radio measurements (up to 60 GHz) of each lobe are separated into two regions, with dark blue data points indicating regions that are closer to the nucleus (regions 2 and 4; see Fig. 2), and light blue points denoting the farther regions (1 and 5). Synchrotron continuum models for each region are overlaid. The component at higher energies is the total IC

emission of each lobe modeled to match the LAT measurements (red points with error bars; error bars indicate 1σ errors). The x-ray limit for the lobe emission derived from *SAS-3* observations (24) is indicated with a red arrow [see (9)]. The break and maximum frequencies in the synchrotron spectra are $\nu_{br} = 4.8$ GHz and $\nu_{max} = 400$ GHz, respectively. νS_ν , frequency multiplied by flux density.

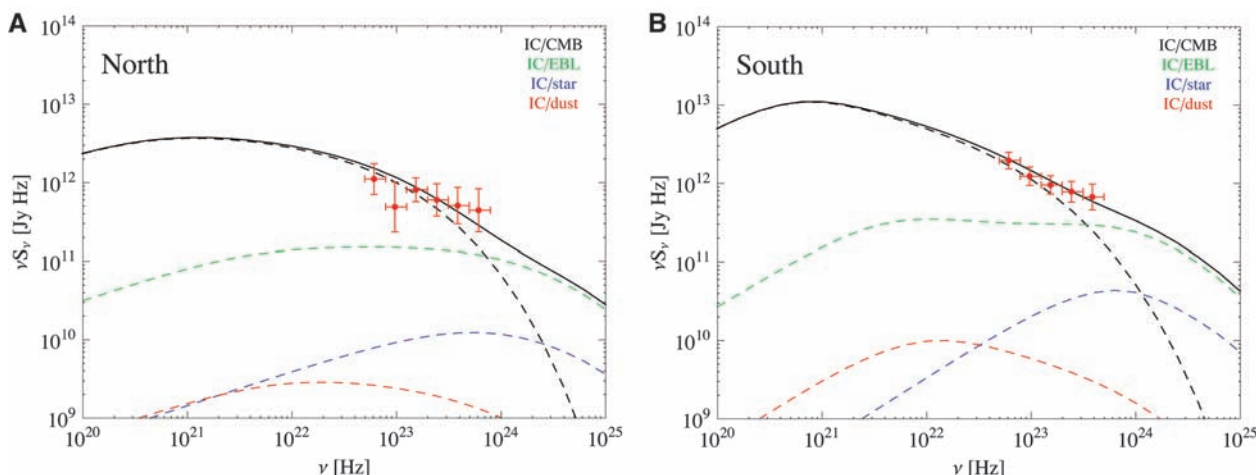


Fig. 4. Detail of the IC portion of the northern (**A**) and southern (**B**) giant lobes' SEDs (Fig. 3). The separate contributions from the different photon seed sources are indicated with dashed lines, and the total emission is

represented by the solid black line. Red data points and error bars are the same as in Fig. 3. Vertical bars indicate errors; horizontal bars indicate frequency range.

To model the observed lobe γ -rays as IC emission, detailed radio measurements of the lobes' synchrotron continuum spectra are necessary to infer the underlying electron energy distribution (EED), $n_e(\gamma)$, where the electron energy is $E_e = \gamma m_e c^2$ (γ , electron Lorentz factor; m_e , electron mass; c , speed of light; n_e , number density of electrons). In anticipation of these Fermi observations, ground-based (16, 17) and WMAP satellite (8) maps of Cen A were previously analyzed (9). Here, we separately fit the 0.4- to 60-GHz measurements for each region defined therein for the north (1 and 2) and south (4 and 5) lobes (Fig. 2) with EEDs in the form of a broken power law (with normalization k_e and slopes s_1 and s_2) plus an exponential cutoff at high energies $n_e(\gamma) = k_e \gamma^{-s_1}$ for $\gamma_{min} \leq \gamma < \gamma_{br}$ and $n_e(\gamma) = k_e \gamma_{br}^{2-s_1} \gamma^{-s_2} \exp[-\gamma/\gamma_{max}]$ for $\gamma \geq \gamma_{br}$, such that the electron energy density is $U_e = \int E_e n_e(\gamma) d\gamma$. To a certain extent, our modeling results depend on the shape of the electron spectrum

at energies higher than those probed by the WMAP measurements ($\nu \geq 60$ GHz) (Fig. 3); we have assumed the spectrum to decline exponentially.

We calculated the IC spectra resulting from the fitted EED (parameters listed in table S1 of the SOM) by employing precise synchrotron (18) and IC (19) kernels (including Klein-Nishina effects) by adjusting the magnetic field B . In addition to the CMB photons, we included IC emission off the isotropic infrared-to-optical extragalactic background light (EBL) radiation field (9, 20, 21), using the data compilation from (22). Anisotropic radiation from the host galaxy starlight and the well-known dust lane was also included, but was found to have a negligible contribution in comparison to the EBL (Fig. 4 and SOM). The resultant total IC spectra of the northern and southern lobes (Fig. 3) with $B = 0.89$ μ G (north) and 0.85 μ G (south) provide satisfactory representations of

the observed γ -ray data. These B -field values imply that the high-energy γ -ray emission detected by the LAT is dominated by the scattered CMB emission, with the EBL contributing at higher energies (≥ 1 GeV) (Fig. 4).

Considering only contributions from ultra-relativistic electrons and magnetic field, the lobe plasma is found to be close to the minimum-energy condition with the ratio of the energy densities $U_e/U_B \approx 4.3$ (north) and ≈ 1.8 (south), where $U_B = B^2/8\pi$. The EED was assumed to extend down to $\gamma_{min} = 1$; adopting larger values can reduce this ratio by a fractional amount for the southern lobe and by up to \sim two times for the northern lobe (SOM). For comparison, IC/CMB x-ray measurements of extended lobes of more powerful [Fanaroff-Riley type-II (23)] radio sources have been used to infer higher B fields and equipartition ratios with a range $U_e/U_B \approx 1-10$ (12-14).

43210, USA. ¹²Istituto Nazionale di Fisica Nucleare, Sezione di Perugia, I-06123 Perugia, Italy. ¹³Dipartimento di Fisica, Università degli Studi di Perugia, I-06123 Perugia, Italy. ¹⁴Dipartimento di Fisica "M. Merlin" dell'Università e del Politecnico di Bari, I-70126 Bari, Italy. ¹⁵Istituto Nazionale di Fisica Nucleare, Sezione di Bari, 70126 Bari, Italy. ¹⁶Laboratoire Leprince-Ringuet, École polytechnique, CNRS/IN2P3, Palaiseau, France. ¹⁷Department of Physics, University of Washington, Seattle, WA 98195–1560, USA. ¹⁸Institut de Ciències de l'Espai (IEEC-CSIC), Campus UAB, 08193 Barcelona, Spain. ¹⁹Istituto Nazionale di Astrofisica (INAF)—Istituto di Astrofisica Spaziale e Fisica Cosmica, I-20133 Milano, Italy. ²⁰Agenzia Spaziale Italiana Science Data Center, I-00044 Frascati (Roma), Italy. ²¹NASA Goddard Space Flight Center, Greenbelt, MD 20771, USA. ²²Center for Research and Exploration in Space Science and Technology and NASA Goddard Space Flight Center, Greenbelt, MD 20771, USA. ²³Department of Physics and Center for Space Sciences and Technology, University of Maryland Baltimore County, Baltimore, MD 21250, USA. ²⁴George Mason University, Fairfax, VA 22030, USA. ²⁵Laboratoire de Physique Théorique et Astroparticules, Université Montpellier 2, CNRS/IN2P3, Montpellier, France. ²⁶Department of Physics and Astronomy, Sonoma State University, Rohnert Park, CA 94928–3609, USA. ²⁷Department of Physics, Stockholm University, AlbaNova, SE-106 91 Stockholm, Sweden. ²⁸The Oskar Klein Centre for Cosmoparticle Physics, AlbaNova, SE-106 91 Stockholm, Sweden. ²⁹Dipartimento di Fisica, Università di Udine and Istituto Nazionale di Fisica Nucleare, Sezione di Trieste, Gruppo Col-

legato di Udine, I-33100 Udine, Italy. ³⁰Université de Bordeaux, Centre d'Études Nucléaires Bordeaux Gradignan, UMR 5797, Gradignan, 33175, France. ³¹CNRS/IN2P3, Centre d'Études Nucléaires Bordeaux Gradignan, UMR 5797, Gradignan, 33175, France. ³²Department of Physical Sciences, Hiroshima University, Higashi-Hiroshima, Hiroshima 739-8526, Japan. ³³Department of Astronomy and Astrophysics, Pennsylvania State University, University Park, PA 16802, USA. ³⁴Department of Physics and Department of Astronomy, University of Maryland, College Park, MD 20742, USA. ³⁵INAF Istituto di Radioastronomia, 40129 Bologna, Italy. ³⁶Max-Planck-Institut für Radioastronomie, Auf dem Hügel 69, 53121 Bonn, Germany. ³⁷Center for Space Plasma and Aeronomic Research, University of Alabama in Huntsville, Huntsville, AL 35899, USA. ³⁸Department of Physics, Royal Institute of Technology, AlbaNova, SE-106 91 Stockholm, Sweden. ³⁹Waseda University, 1-104 Totsukamachi, Shinjuku-ku, Tokyo, 169-8050, Japan. ⁴⁰Department of Physics, Tokyo Institute of Technology, Meguro City, Tokyo 152-8551, Japan. ⁴¹Cosmic Radiation Laboratory, Institute of Physical and Chemical Research (RIKEN), Wako, Saitama 351-0198, Japan. ⁴²Centre d'Étude Spatiale des Rayonnements, CNRS/UPS, BP 44346, F-30128 Toulouse Cedex 4, France. ⁴³Istituto Nazionale di Fisica Nucleare, Sezione di Roma "Tor Vergata," I-00133 Roma, Italy. ⁴⁴Department of Physics and Astronomy, University of Denver, Denver, CO 80208, USA. ⁴⁵Max-Planck Institut für Extraterrestrische Physik, 85748 Garching, Germany. ⁴⁶Institut für Astro- und Teilchenphysik and Institut für Theoretische Physik, Leopold-Franzens-Universität Innsbruck, A-6020 Innsbruck,

Austria. ⁴⁷Space Sciences Division, NASA Ames Research Center, Moffett Field, CA 94035–1000, USA. ⁴⁸NYCB Real-Time Computing, Lattingtown, NY 11560–1025, USA. ⁴⁹Astronomical Observatory, Jagiellonian University, 30-244 Kraków, Poland. ⁵⁰Department of Chemistry and Physics, Purdue University Calumet, Hammond, IN 46323–2094, USA. ⁵¹Institute of Space and Astronautical Science, Japanese Aerospace Exploration Agency, 3-1-1 Yoshinodai, Sagami-hara, Kanagawa 229-8510, Japan. ⁵²Institució Catalana de Recerca i Estudis Avançats, Barcelona, Spain. ⁵³Consorzio Interuniversitario per la Fisica Spaziale, I-10133 Torino, Italy. ⁵⁴Dipartimento di Fisica, Università di Roma "Tor Vergata," I-00133 Roma, Italy. ⁵⁵School of Pure and Applied Natural Sciences, University of Kalmar, SE-391 82 Kalmar, Sweden. ⁵⁶Centre for Astrophysics Research, University of Hertfordshire, College Lane, Hatfield AL10 9AB, UK.

Supporting Online Material

www.sciencemag.org/cgi/content/full/science.1184656/DC1
Materials and Methods

SOM Text

Figs. S1 to S3

Tables S1 to S3

References

13 November 2009; accepted 19 March 2010

Published online 1 April 2010;

10.1126/science.1184656

Include this information when citing this paper.

The Equation of State of a Low-Temperature Fermi Gas with Tunable Interactions

N. Navon,*† S. Nascimbène,* F. Chevy, C. Salomon

Interacting fermions are ubiquitous in nature, and understanding their thermodynamics is an important problem. We measured the equation of state of a two-component ultracold Fermi gas for a wide range of interaction strengths at low temperature. A detailed comparison with theories including Monte-Carlo calculations and the Lee-Huang-Yang corrections for low-density bosonic and fermionic superfluids is presented. The low-temperature phase diagram of the spin-imbalanced gas reveals Fermi liquid behavior of the partially polarized normal phase for all but the weakest interactions. Our results provide a benchmark for many-body theories and are relevant to other fermionic systems such as the crust of neutron stars.

Recently, ultracold atomic Fermi gases have become a tool of choice to study strongly correlated quantum systems because of their high controllability, purity, and tunability of interactions (*I*). In the zero-range limit, interactions in a degenerate Fermi system with two spin-components are completely characterized by a single parameter $1/k_F a$, where *a* is the *s*-wave scattering length and $k_F = (6\pi^2 n)^{1/3}$ is the Fermi momentum (*n* is the density per spin state). In cold atom gases, the value of $|a|$ can be tuned over several orders of magnitude using a Feshbach resonance; this offers an opportunity to entirely explore the so-called BCS-BEC crossover, that is, the smooth transition from Bardeen-Cooper-Schrieffer (BCS) superfluidity at small

negative values of *a* to molecular Bose-Einstein Condensation (BEC) at small positive values of *a* (*I*, 2). Between these two well-understood limiting situations, *a* diverges, leading to strong quantum correlations. The description of this system is a challenge for many-body theories, as testified by the large amount of work in recent years (*I*). The physics of the BEC-BCS crossover is relevant for very different systems, ranging from neutron stars to heavy nuclei and superconductors.

In the grand-canonical ensemble and at zero temperature, dimensional analysis shows that the Equation of State (EoS) of a two-component Fermi gas, relating the pressure *P* to the chemical potentials μ_1 and μ_2 of the spin components can be written as

$$P(\mu_1, \mu_2, a) = P_0(\mu_1) h \left(\delta_1 \equiv \frac{\hbar}{\sqrt{2m\mu_1} a}, \eta \equiv \frac{\mu_2}{\mu_1} \right) \quad (1)$$

where $P_0(\mu_1) = 1/15\pi^2 (2m/\hbar^2)^{3/2} \mu_1^{5/2}$ is the pressure of a single-component ideal Fermi gas,

m is the atom mass, \hbar is the Planck constant divided by 2π , and δ_1 is the grand-canonical analog of the dimensionless interaction parameter $1/k_F a$. The indices 1 and 2 refer to the majority and minority spin components, respectively. From the dimensionless function $h(\delta_1, \eta)$, it is possible to deduce all the thermodynamic properties of the gas, such as the compressibility, the magnetization, or the existence of phase transitions. The aim of this paper is to measure $h(\delta_1, \eta)$ for a range of interactions (δ_1) and spin imbalances (η) and discuss its physical content. Because it contains the same information as Eq. 1, the function *h* will also be referred to as the EoS in the rest of the text.

In situ absorption images of harmonically trapped gases are particularly suited to investigate the EoS, as first demonstrated in (3) and (4). In the particular case of the grand-canonical ensemble, a simple formula relates the local pressure *P* at a distance *z* from the center of the trap along the *z* axis to the doubly integrated density profiles \bar{n}_1 and \bar{n}_2 (5).

$$P(\mu_1(z), \mu_2(z), a) = \frac{m\omega_r^2}{2\pi} (\bar{n}_1(z) + \bar{n}_2(z)) \quad (2)$$

Here, we define the local chemical potentials $\mu_i(z) = \mu_i^0 - \frac{1}{2} m\omega_z^2 z^2$, where μ_i^0 is the chemical potential of the component *i* at the bottom of the trap, assuming local density approximation. ω_r and ω_z are the transverse and axial angular frequencies of a cylindrically symmetric trap, respectively, and $\bar{n}_i(z) = \int n_i(x, y, z) dx dy$ is the atomic density *n_i* of the component *i*, doubly integrated over the transverse *x* and *y* directions. In a single experimental run at a given magnetic field, two images are recorded, providing $\bar{n}_1(z)$ and $\bar{n}_2(z)$ (fig. S4); the *z*-dependence of the chemical potentials then enables the measurement of *P* along a curve in the (δ_1, η) plane (6). This method was validated in (4) for the particular case of the

Laboratoire Kastler Brossel, CNRS, Université Pierre et Marie Curie, École Normale Supérieure, 24 rue Lhomond, 75231 Paris, France.

*These authors contributed equally to this work.

†To whom correspondence should be addressed. E-mail: navon@ens.fr